Document downloaded from:

http://hdl.handle.net/10251/84613

This paper must be cited as:

Guzmán-Afonso, C.; León-Luis, S.; Sans-Tresserras, JÁ.; González -Silgo, C.; Rodríguez-Hernández, P.; Radescu, S.; muñoz, A.... (2015). Experimental and theoretical study of –Eu2(MoO4)3 under compression. Journal of Physics: Condensed Matter. 27(46):465401-1-465401-11. doi:10.1088/0953-8984/27/46/465401.

The final publication is available at

http://dx.doi.org/10.1088/0953-8984/27/46/465401

Copyright IOP Publishing

Additional Information

Experimental and theoretical study of α–$Eu_2(MoO_4)_3$ under compression

C. Guzmán-Afonso[1], S. F. León-Luis[1,2,3], J. A. Sans[3,4], C. González-Silgo[1,2,3], P. Rodríguez-Hernández[1,2,3], S. Radescu[1,2,3], A. Muñoz[1,2,3], J. López-Solano[1,2,5], D. Errandonea[3,6], F. J. Manjón[3,4], U. R. Rodríguez-Mendoza[1,2,3], and V. Lavín[1,2,7]

[1] Dpto. de Física, Universidad de La Laguna, 38200 La Laguna, Tenerife, Spain
[2] Instituto de Materiales y Nanotecnología, Universidad de La Laguna
[3] MALTA Consolider Team
[4] Instituto de Diseño para la Fabricación y Producción Automatizada, Universidad Politécnica de Valencia, 46022 Valencia, Spain
[5] Izaña Atmospheric Research Center, Agencia Estatal de Meteorología, Tenerife, Spain
[6] Dpto. de Física Aplicada, 46100 Burjassot, Valencia, Spain
[7] Instituto de Estudios Avanzados en Atómica, Molecular y Fotónica, Universidad de La Laguna

E-mail: mcguzman@ull.es

Abstract. The compression process in the α-phase of europium trimolybdate was revised employing several experimental techniques. X-ray diffraction using synchrotron and laboratory radiation sources, Raman scattering and photoluminescence experiments were performed up to a maximum pressure of 21 GPa. In addition, the crystal structure and Raman mode frequencies have been studied by means of first-principles density functional based methods. Results suggest that the compression process of α-$Eu_2(MoO_4)_3$ can be described by three stages. Below 8 GPa, the α-phase suffers an isotropic contraction of the crystal structure. Between 8 and 12 GPa, the compound undergoes an anisotropic compression due to distortion and rotation of the MoO_4 tetrahedra. At pressures above 12 GPa, the amorphization process starts without any previous occurrence of a crystalline-crystalline phase transition in the whole range of pressure. This behavior clearly differs from the process of compression and amorphization in trimolybdates with β'-phase and tritungstates with α-phase.

PACS numbers: 61.05.cp, 78.55.Hx, 31.15.A-, 63.20.-e

Keywords: High pressure; X-ray diffraction; Raman scaterring, Photoluminescence

Submitted to: *J. Phys.: Condens. Matter*

1. Introduction

Trimolybdates and tritungstates with chemical formula $RE_2(MO_4)_3$ (RE=rare earth; M=Mo, W) are a large group of important materials from both the fundamental and technological points of view. They include several polymorphic materials which are mainly used as scintillators in high energy physics [1], outer space and medical diagnostic devices. They are also good phosphors due to the fluorescence of the majority of the RE ions [2]. In addition, crystals containing Eu^{3+} ions are of particular interest because these ions produce the efficient red photoluminescence necessary for the creation of white-light emitting diodes [3].

For rare earths with intermediate ionic radii (from Sm to Dy), the two structural phases of these families of compounds at ambient conditions are the α-phase [4], with space group *C2/c* and modulated scheelite-type structure [5], and the β'-phase [6], with space group *Pba2* and which only occurs for trimolybdates [7]. Therefore, europium trimolybdate can adopt either phase, depending on the crystallization conditions. This polymorphism makes these compounds good prototypes to understand concepts related to the physics of pressure-induced phase transitions and amorphization processes.

Further studies have been conducted to investigate the compression of the β'-phase than the α-phase in trimolybdates. These studies have revealed that the pressure-induced amorphization (PIA) in β'-phase compounds is irreversible and occurs at about 4 GPa [8–10]. Moreover, before the PIA is reached, a phase transition to a δ-phase may take place [11]. However, Raman scattering measurements dating back several decades have evidenced that α-phase compounds, like $Nd_2(MoO_4)_3$ and $Tb_2(MoO_4)_3$, undergo a partially reversible PIA at 13 and 18 GPa, respectively [12]. More recently, PIA in both α- and β'-phases has been explained as a spatial self-organization of the oxygen clouds around the Mo and RE subnetworks despite their different behaviors before amorphization occurs [13, 14]. On the other hand, the compression of α-phases in $La_2(WO_4)_3$ and $Tb_2(MoO_4)_3$ has been analyzed in depth very recently [11, 15]. It has been found that the first compound undergoes two phase transitions prior to PIA [15], while the second one reach the amorphization without phase transitions [11].

In this work, we focus on the study of the compression of α-$Eu_2(MoO_4)_3$ in order to reach a better understanding of the PIA mechanisms in tritungstates and trimolybdates with α-phase, to analyze both the differences between the two families of compounds, and between the α- and β'- phases. X-ray diffraction using synchrotron and laboratory radiation sources, Raman scattering, and photoluminescence experiments were performed in polycrystalline samples. The utilization of these three experimental techniques allows us to compare our results from ambient pressure with those of a very recent work about α-$Eu_2(MoO_4)_3$ [16]. In addition, *ab initio* calculations were carried out to complement our experimental results. The combination of all these methods has allowed us to provide a more comprehensive and complete picture of the structural (both at long and short range) and of vibrational behavior at high pressure of the α-phase in trimolybdates. We expect our results to complement previous Raman and XAS studies

(combined with numerical simulations) in $Eu_2(MoO_4)_3$ by Le Bacq *et al* [13], which were mainly focused on the β'-phase. In addition, because the photoluminescence of the β'-phase has been previously studied under pressure in great detail [17], we also present here a similar analysis for the α-phase. This is required to clearly establish the differences in the behavior under pressure of these two polymorphs of $Eu_2(MoO_4)_3$.

2. Experimental and theoretical details

The sample of α-$Eu_2(MoO_4)_3$ was prepared by conventional solid-state synthesis (see Ref. [18] for more details). The polycrystalline powder was measured at room temperature by two X-ray diffractometers. On the one hand, we employed a synchrotron radiation source (λ=0.485 Å) equipped with a MAR345 CCD detector at the *Beamline I15* of the Diamond Light Source. On the other hand, we used a conventional SuperNova diffractometer (Kα molybdenum radiation) equipped with a 135-mm Atlas CCD detector at the "Servicio Integrado de Difracción de Rayos X (SIDIX)" of the University of La Laguna. Pressures reached in the synchrotron experiment, up to 14.6 GPa, were generated with a MiniDac-type diamond anvil cell (DAC), with an aperture angle of 40^o and designed at the University of Paderborn in Germany, using Dow Corning silicone oil as pressure-transmitting medium. The diamond culet size was 400 μm, and the chamber size was 300 μm in diameter and 50 μm in thickness. Pressures reached in the conventional experiment, up to 5.3 GPa, were generated with a Diacell Bragg-Mini DAC (with aperture angle of 85^o) using a mix of methanol-ethanol-water 16:3:1 as pressure-transmitting medium. The diamond culet size was 500 μm, and the chamber size was 200 μm in diameter and 100 μm thickness. In both experiments, the in-situ pressure was measured using the ruby fluorescence technique [19], with the pressure scale recalibrated by Mao *et al* [20], and the observed intensities were integrated as a function of the 2θ angle using the Fit2D software [21]. The 1D-diffraction patterns were refined by iterating full pattern profile fittings with the Le Bail method [22], using the FullProf software [23] and starting from the crystallographic cell obtained in Ref. [16]. The background was modeled by a linear interpolation between points. Besides, the lattice parameters, the half-width parameter, related to the Gaussian broadening of the peaks due to isotropic microstrains, were also refined. Above 4.7 GPa, anisotropic broadening and shifts of some reflections were detected systematically (only in the data measured in the synchrotron experiment) and they were refined too.

Raman scattering measurements of powder α-$Eu_2(MoO_4)_3$ samples at room temperature were performed in backscattering geometry, exciting with a HeNe laser at 632.8 nm with an incident power of 10 mW and using a HORIBA Jobin Yvon LabRAM HR UV spectrometer in combination with a thermoelectrically cooled multichannel CCD detector with a resolution below 2 cm^{-1}. The background of the experimental Raman spectra was subtracted and vibrational modes were analyzed by fitting the Raman peaks with a Voigt profile. The beam was focused on the sample using a 50× objective with a beam diameter of approximately 2 μm at the sample. For high-pressure Raman

measurements, the sample was placed in a membrane-type DAC. The diamond culet size was 400 μm and the gasket hole size was 150 μm. A mixture of methanol-ethanol-water (16:3:1) was used in this case as a pressure-transmitting medium and the pressure was measured using the same method we used in the diffraction experiment.

Room-temperature fluorescence spectra of Eu^{3+} ions in α-$Eu_2(MoO_4)_3$ were excited with a 405 nm laser diode and recorded with a Spex 75 cm monochromator equipped with Hamamatsu R928 photomultiplier tubes (spectral resolution of 0.1 nm). High-pressure measurements were carried out at room temperature in a pressure range from 0 to 14.6 GPa, using the same Mini-DAC as in the diffraction experiment, and a mixture of methanol-ethanol-water (16:3:1). Pressures were determined by the ruby fluorescence method, as in the previous experiments.

First-principles total-energy calculations were performed within the framework of the density-functional theory (DFT) [24] using the Vienna *ab initio* simulation package (VASP) [25, 26]. Calculations were carried out with the pseudopotential method and the projector augmented wave (PAW) scheme [27]. The exchange-correlation energy was taken in the generalized gradient approximation (GGA) with the PBEsol [28] prescription. We used the GGA+U (U=4 eV) method to account for the strong correlation between the Eu f electrons on the basis of Dudarev's method [29]. Highly converged results were achieved by extending the set of plane waves up to a kinetic energy cutoff of 520 eV. A dense Monkhorst-Pack grid of 3×3×2 k-special points was used to perform integrations along the Brillouin zone (BZ) in order to obtain thoroughly converged energies and forces. The structural configurations were fully relaxed at each volume through the calculation of the forces on atoms and the components of the stress tensor [30]. In the relaxed configurations, the forces on the atoms were less than 0.006 eV/Å and deviations of the stress tensor from a diagonal hydrostatic form, less than 0.1 GPa. It should be noted that, in the DFT formalism, the theoretical pressure P(V) is obtained from the calculated stress [31]. Zero point motion and temperature effects were not included in the calculations.

Lattice-dynamics calculations were performed at the zone center (Γ point) of the BZ using the direct force constant (or supercell) approach [32]. The construction of the dynamical matrix at the Γ point of the BZ involves separate calculations of the forces in which a fixed displacement from the equilibrium configuration of the atoms within the primitive cell is considered. The diagonalization of the dynamical matrix allows to obtain the frequencies of the Raman modes. Moreover, these calculations allow for the identification of the symmetry and eigenvectors of the vibrational modes in each structure at the Γ point.

3. Results and discussion

3.1. Pressure dependence of the lattice parameters

Fig. 1 shows a selection of diffraction patterns of $Eu_2(MoO_4)_3$ up to 14.6 GPa. The background has been subtracted and the diffraction patterns have been normalized in order to improve their visualization. All reflections of the initial diffractogram, at an ambient pressure (AP) of 1 atm, correspond to the expected ones for α-$Eu_2(MoO_4)_3$, i.e. we did not observe any reflections from impurities. The most notable feature of these diffractograms is that the widths of some reflections start to increase above 4.7 GPa. For instance, this effect is clearly visible for the reflection with Miller indices (0 0 2) located at 5.1^o (see the asterisk in Fig. 1). In addition, some of these reflections show a systematic shift to lower angles with increasing pressure. Both effects can be due to an excessive number of crystal grains loaded in the DAC, so that the grains are subjected to non-hydrostatic stresses. This would result in a non-uniform strain within a grain (microstrain) or/and over larger distances (macrostrain), producing the peak broadening and shifting, respectively. In spite of this possible non-hydrostatic condition of the sample, we did not observe any phase transition in the whole pressure range of the synchrotron experiment. This result is in agreement with our own (see section 3.3) and previous Raman studies [13]. The same behavior has been found in isostructural α-$Tb_2(MoO_4)_3$ pressurized up to 20.74 GPa [11]. Based on the results of these two isostructural compounds, we expect the same behavior for all RE trimolybdates with α-phase, i.e. the sequence of trimolybdates with RE from samarium to dysprosium.

The bottom diffractogram of Fig. 1, marked with an R and corresponding to the release from high pressure, is similar to the diffractogram measured at AP, although the peaks are slightly wider. This broadening can be due to the non-hydrostatic stresses that remain in the sample after release of pressure. Overall, it can be concluded that the compression of the cell up to 14.6 GPa is a reversible process.

In order to obtain more information about the behavior of α-$Eu_2(MoO_4)_3$ under pressure, we refined all diffractograms collected up to 11.6 GPa and also the one obtained after decompression. These refinements are displayed as black lines in Fig. 1. The refinements were not performed at pressures larger than 11.6 GPa due to the broadening of the reflections. The experimental pressure dependence of the lattice parameters, the monoclinic β angle, and the volume were obtained from these refinements. The pressure evolution of these five parameters are plotted in Fig. 2, together with the theoretical lattice parameters calculated by *ab initio* methods. Note that a reasonable agreement is found between experimental data from synchrotron and conventional radiation source. Moreover, the theoretical data reproduce the experimental behavior of the lattice parameters. When pressure increases, b and c lattice parameters decrease monotonously, whereas a parameter suffers a contraction up to 8 GPa. After that pressure, its value increases smoothly, remaining constant after 12 GPa according to the *ab initio* calculations. The monoclinic angle β increases with pressure, suffering an abrupt increment on its slope above 8 GPa and up to 12 GPa. Although the compression

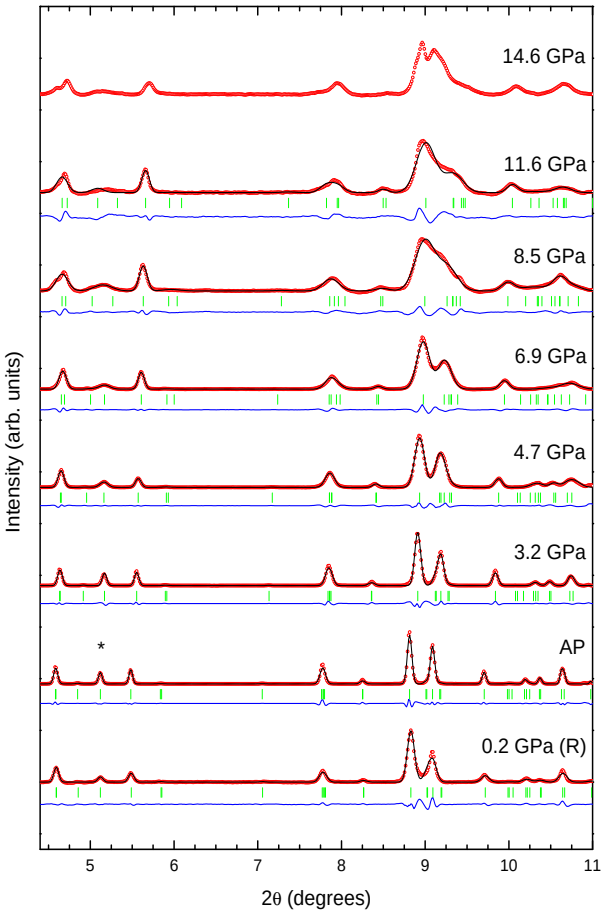

Figure 1. Diffraction patterns of α-$Eu_2(MoO_4)_3$ at selected pressures of the synchrotron experiment. Experimental results (red circles) are shown together with the calculated patterns (black lines) and residuals (blue lines). The ticks indicate the positions of Bragg reflections. Pressures are indicated in the figure. The patterns labeled as AP and R were collected at ambient pressure and at 0.2 GPa after pressure release, respectively.

behavior of the *a* parameter is remarkably different than that of the other parameters, the volume decreases monotonically. This unusual dependence with pressure of the *a* parameter is similar to that found in α-$Tb_2(MoO_4)_3$, although in this latter compound the monoclinic angle decreases with increasing pressure [11].

We have fitted the calculated data up to 12.2 GPa with a third order Birch-Murnaghan equation of state (EOS), obtaining V_0=950.6(6) Å^3, B_0=63(1) GPa, and B'_0=3.7(2). We also used the previous equation to fit the experimental data up to 11.6 GPa, obtaining V_0=941.41(6) Å^3, B_0=88(4) GPa and B'_0=6(1). Thus, the pressure evolution of the experimental volume shows a larger bulk modulus than the one inferred from the theoretical data, so that the sample is not as compressible as the theoretical data predict. We believe that this difference is probably related to the excessive number of crystal grains loaded into the chamber, causing the mentioned anisotropic stress on the sample and decreasing the compressibility of the crystal structure as Errandonea

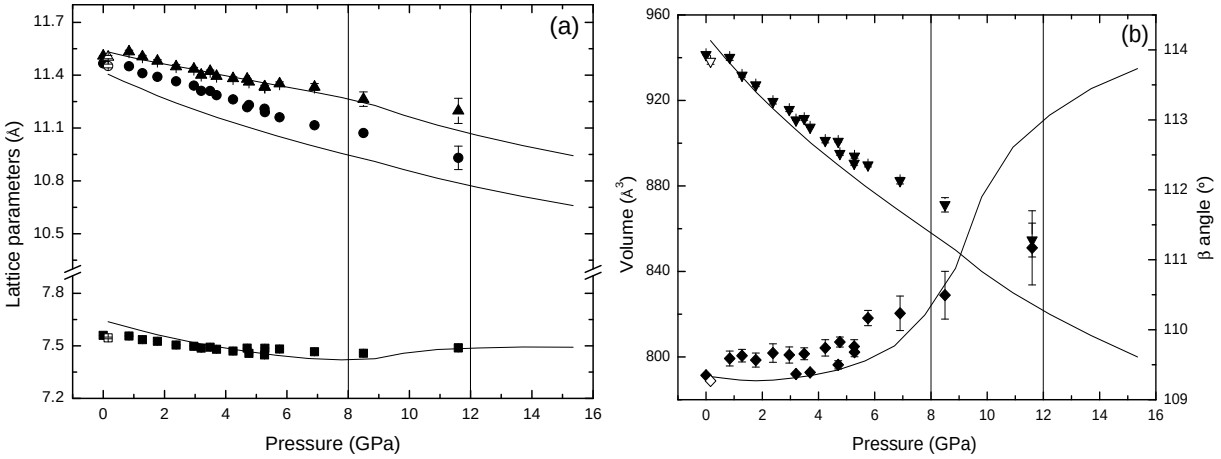

Figure 2. Pressure dependence of experimental (solid symbols, data estimated from measurements at with both synchrotron and conventional radiation sources) and theoretical (black lines) lattice parameters for α-$Eu_2(MoO_4)_3$. The left panel shows the a (■), b (●), and c (▲) lattice parameters. The right panel shows the volume (▼) and the β angle (♦). Lines are a guide to the eye and error bars represent the standard deviations. Experimental lattice parameters were refined using data from both synchrotron (up to 11.6 GPa) and conventional (up to 5.3 GPa) experiments. Empty symbols are experimental data upon decompression. Vertical lines are used to distinguish three regions with different tendency.

et al [33] explain. The difference found between the theoretical and experimental bulk modulus can also be due to the influence of the pressure-transmitting medium [34]. In particular in scheelite-type compounds it is well known that the utilization of a pressure-transmitting medium different than Ne or He tends to underestimate the compressibility (overestimate bulk modulus) [35, 36]. On the other hand, the difference between theoretical and experimental volume is most likely related to the usual overestimation of the equilibrium volume (which leads to an underestimation of the bulk modulus) produced by the GGA exchange-correlation approximation [31]. We have also calculated the bulk modulus for α-$Tb_2(MoO_4)_3$ using the data provided in Ref. [11]. The obtained values are 76(1) and 81(9) GPa for the theoretical and experimental bulk modulus, respectively, and both are quite close to the present experimental result.

3.2. Structural compression

Using the data provided by our theoretical calculations, we now analyze the structural mechanisms that cause the abrupt changes observed between 8 and 12 GPa [12, 13]. Using the theoretical atomic coordinates and the program BondStr [23, 37], we have calculated bond distances and angles, bond valence sum [37] around the cations, and the distortion of the EuO_8 polyhedra by compression. We have plotted the difference between the bond valence sums for cations and their corresponding oxidation number in Fig. 3(a). As shown, this value increases for Eu ion in the whole range of pressures. However, the behavior for the Mo ions is markedly different, with a change of tendency

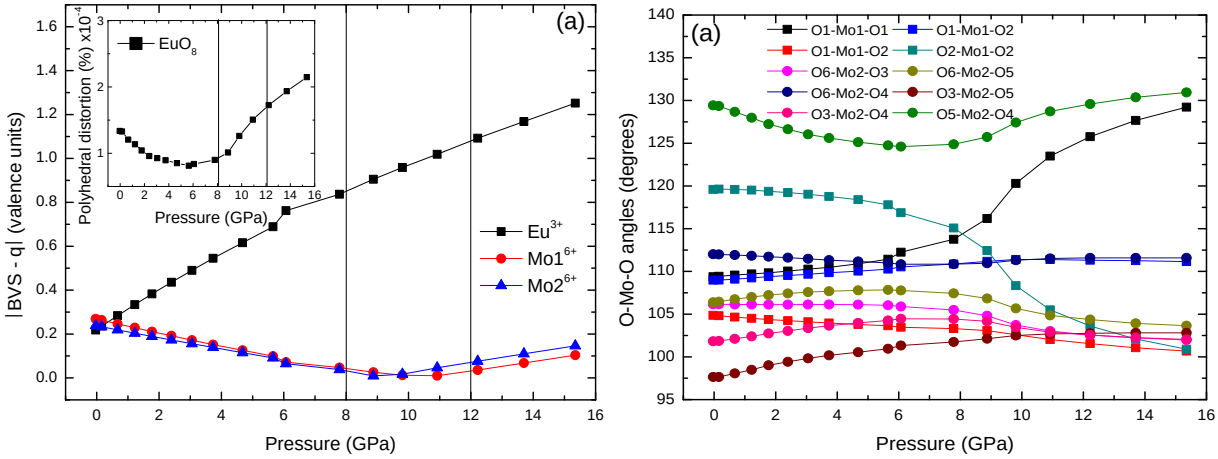

Figure 3. (a) Pressure evolution of the difference between bond valence sums and the oxidation number for the Eu^{3+}, $Mo1^{6+}$ and $Mo2^{6+}$ ions. The inset shows the polyhedral distortion for EuO_8 at different pressures. (b) Eu–O–Mo bridging angles as a function of pressure. Vertical lines are used to distinguish three regions with different tendency.

(turnaround) in the pressure dependence at 10 GPa. These values decrease at lower pressure, allowing a compensation between the increase of the valence in the Eu ion and the decrease of the valences in the Mo ions. We also show the polyhedral distortion of EuO_8 in the inset of Fig. 3. This distortion has an abrupt change at about 10 GPa, coinciding with the minimum value of the bond valence sum for the Mo^{6+} cations, favoring the increase of the bond valence sum for the Eu^{3+} cation. Overall, the changes of tendency in the bond valence sums and polyhedral distortion happen between 8 and 12 GPa, as it is also observed for the cell parameters. At higher pressures, all bond valence sums and polyhedral distortion increase faster and this may have an effect on the structural stability.

In order to correlate the pressure dependence of the polyhedral bond distances and angles with the evolution of lattice parameters under pressure, we have also plotted in Fig. 3(b) the angles of the oxygen bridges Eu–O–Mo which connect all the crystal structure. Note that the atom labels have been assigned using the same criterion as in Ref. [38]. We will discuss these curves together with Figs. 4 and 5, where different views of the crystal structure of the α-phase are drawn. Note that in these figures, we have plotted the atomic coordinates at three selected pressures, *viz.*, 0, 7.8 and 12.2 GPa. In Fig. 4 we can see that both MoO tetrahedra rotate anticlockwise along the b-axis and slightly deform as pressure increases. Therefore the tetrahedra are more aligned along the a axis (colored in red in Fig. 4) at 12.2 GPa, forming a more compact crystal packing. We can go even further in our description of the pressure effect on the α-phase, and explain the decrease of the a parameter as a result of the rotation and deformation of the MoO tetrahedra, up to a pressure when the alignment along the a-axis is reached. After this, the a parameter increases up to a pressure where it becomes constant. Moreover, the β-angle increases following the anticlockwise rotation

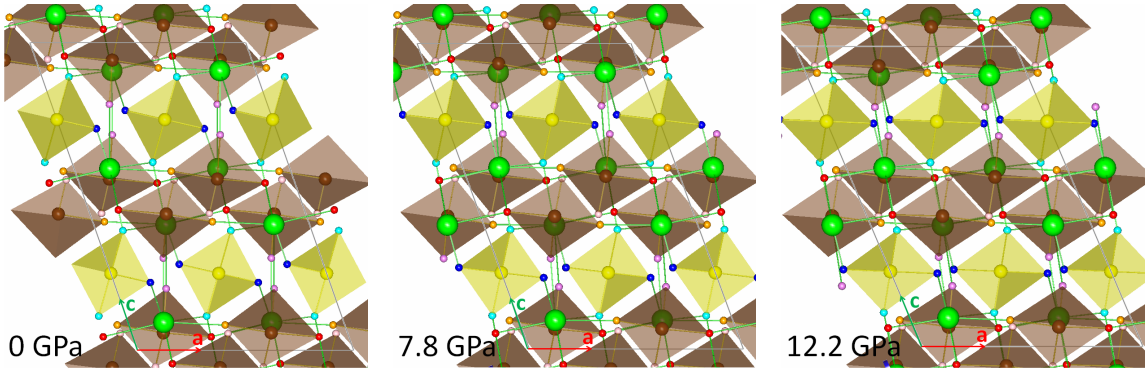

Figure 4. View along the *b*-axis of the α-$Eu_2(MoO_4)_3$ structure at three selected pressures. Europium cations are shown in green. Molybdenum atoms and their coordination tetrahedra are yellow for Mo1, and brown for Mo2. The oxygen atoms are shown in dark blue (O1), cyan (O2), violet (O3), red (O4), orange (O5) and pink (O6).

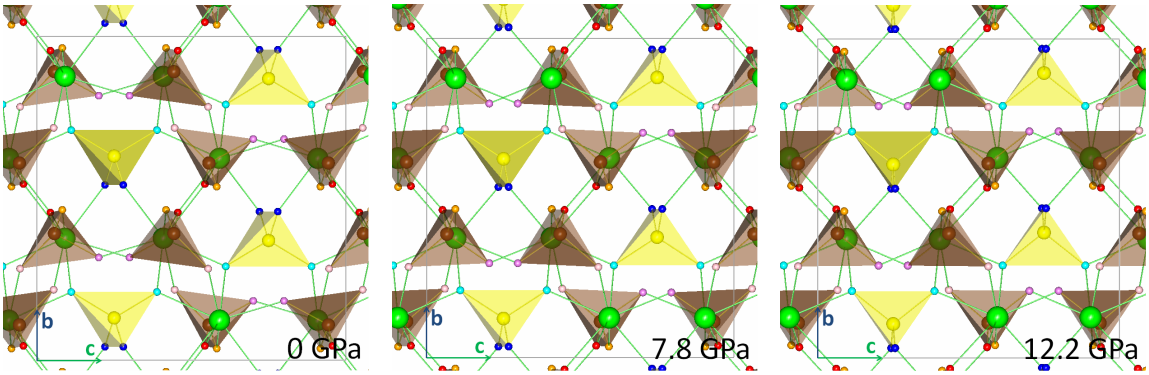

Figure 5. Same as Fig. 4 but showing a view along the *a*-axis.

of the MoO_4 tetrahedra. This increase is also observed in $La_2(WO_4)_3$ [15] up to the first pressure-induced phase transition, while in $Tb_2(MoO_4)_3$ the opposite behavior is observed [11], with tetrahedra undergoing a clockwise rotation in the pressure range from 7.5 to 12.7 GPa. The evolution of all the oxygen-bridge angles (see Fig. 3(b)) helps to explain the rotation and deformation of both tetrahedra and therefore the unusual compression of the cell parameters. The more drastic contraction occurs for the angles Eu–O1–Mo1, Eu–O3–Mo2 and Eu–O6–Mo2. The changes in these bridges must be thus the major reason for the alignment of both tetrahedra. This is best shown in Fig. 5, where it can be observed the alignment of the O1 atoms along the *a*-axis, and of the O3 and O6 oxygens along the *c*-axis (colored in green in Fig. 5). Furthermore, note that the experimental results from X-ray diffraction show that the broadening of the patterns is almost recovered at ambient pressure, as it also happens in other trimolybdates with *α*-phase [12, 13]. This may be the result of the reversibility of the rotations and deformations of the MoO_4 groups described above. Note that this is not

the case of $La_2(WO_4)_3$ and probably other light RE tritungstates with the α-phase, where vacancies and RE atoms are disordered and the structure is not recovered at ambient conditions [15].

3.3. Vibrational properties

Raman spectra obtained during compression of the α-$Eu_2(MoO_4)_3$ phase up to 21 GPa are shown in Fig. 6(a). These spectra show a large number of Raman modes. This is in agreement with the theoretical modes of the α-phase, and the analysis performed in Ref. [16] (see Table 1). Note that two fluorescence bands of the Eu^{3+} ion at 511 and 634 cm^{-1} are inside this energy gap, and thus are located at a range where they will have a small effect on the detection of Raman peaks close to them. These kind of peaks were also detected by Dmitriev *et al* [9].

Besides the expected upshift of the Raman peaks with increasing pressure, we did not observed abrupt changes in the Raman spectra up to 8.3 GPa. This is in agreement with previous results for the α-phase of $Nd_2(MoO_4)_3$, $Tb_2(MoO_4)_3$, and $Eu_2(MoO_4)_3$ [12, 13]. Above 8.3 GPa, a slight splitting of the high-frequency modes was observed, likely related to a minor structural change which results in an anomalous behavior in the a parameter and β angle. This splitting was also observed in Ref. [13], but not in the other aforementioned studies, in which pressure was increased in larger steps [12]. Moreover, we have observed the onset of PIA above 21 GPa, as in Ref. [13]. This amorphization pressure is higher than that of $Nd_2(MoO_4)_3$ (13 GPa) and $Tb_2(MoO_4)_3$ (18 GPa) [12]. This seems to suggest that a clear correlation between the amorphization pressure and the RE ionic radii cannot be established. However, we must note that the Raman spectrum of $Nd_2(MoO_4)_3$ in Ref. [12] likely corresponds to a $La_2(MoO_4)_3$-type structure, which is also a modulated scheelite-type structure, but not isostructural to the α-phase.

Fig. 6(b) shows the pressure dependence of the experimental Raman mode frequencies on upstroke to 20 GPa (full symbols) which are compared with the theoretical results (solid lines). Up to 8.3 GPa, most of the Raman peaks of the α-phase exhibit a monotonic shift of frequency which is consistent with the general contraction of the unit-cell parameters shown by our X-ray diffraction measurements. Overall, in this range of pressures, the experimental Raman modes are in reasonable agreement with the ones obtained in our calculations, without a clear experimental increase or decrease of the number of Raman modes.

The three frequency regions corresponding to the original α-phase are present in all the pressures measured [16], with similar pressure dependence and experimental-theoretical correspondence. However, some anomalies, more clearly seen in the theoretical calculations, can be discussed on the basis of the observed and calculated compression of the crystal structure. Several stretching modes soften (exhibit negative pressure coefficients) between 8 and 12 GPa. This behavior can be observed experimentally at least in the second highest frequency mode above 10.9 GPa and it

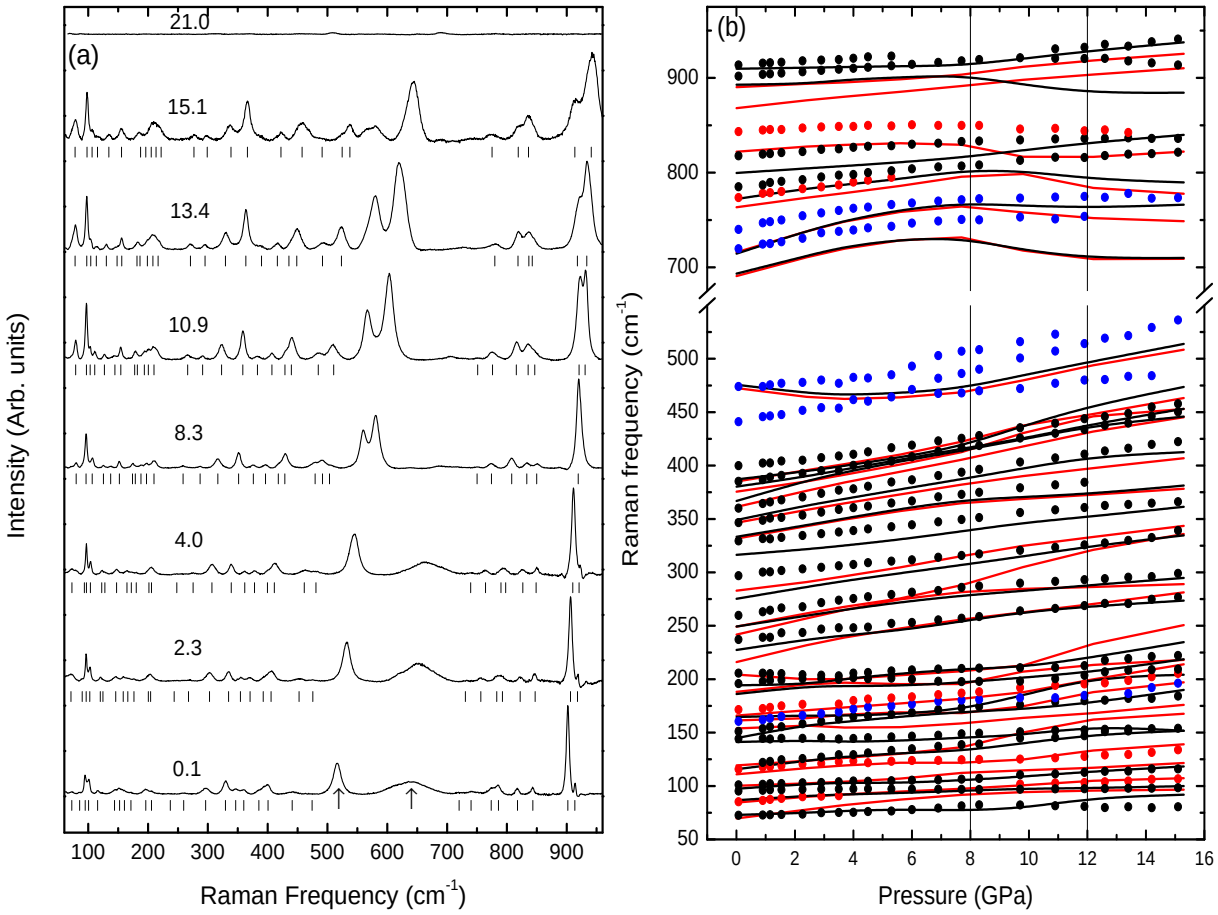

Figure 6. (a) Selection of Raman spectra and (b) pressure dependence of the Raman mode frequencies in α-$Eu_2(MoO_4)_3$ according to our experiments (circles) and theoretical calculations (lines). Next to each spectrum we give the pressure (in GPa) measured using the ruby fluorescence method. Ticks indicate the peak positions. The arrows denote Eu^{3+} fluorescence bands. Different colors have been used to denote the symmetry of the Raman modes: black for Ag, red for Bg, and blue for modes without assigned symmetry or second order modes. Vertical lines in the right panel are used to distinguish the three regions with different tendency.

can be correlated with the unusual behavior of the a parameter, and the beginning of the distortion of the tetrahedra. This trend changes above 12 GPa, coinciding with the alignment of the tetrahedra along the a-axis and the consequent small compression of the a parameter. With respect to the bending-modes region, a slight change of the slope is observed between 8 and 12 GPa, and again it can be related to the start of the tetrahedral distortion. As regards the region of the external modes, this is the most difficult region to analyze since there are a lot of Raman modes whose frequencies overlap. Several Raman modes change their pressure coefficients near 8 GPa; however, this feature is barely detected in our experiments. The analysis is even more difficult at pressures beyond 12 GPa because the broadening of peaks gives rise to their overlapping. This likely related to the development of the PIA.

The Raman spectrum of $Eu_2(MoO_4)_3$ correlate well with the pressure coefficients

Table 1. Theoretical (th.) and experimental (exp.) Raman-active mode frequencies (ω_0, in cm^{-1}) and pressure coefficients ($\partial\omega/\partial p$, in cm^{-1}/GPa) in α-$Eu_2(MoO_4)_3$ at lower pressures (<3 GPa).

Sym.	ω_0 (th.)	$\partial\omega/\partial p$ (th.)	ω_0 (exp.)	$\partial\omega/\partial p$ (exp.)	ω_0 (exp.)[a]
Bg^1	69.6	3.2	—	—	52.6
Ag^1	73.0	0.9	72.6	0.8	59.2
Bg^2	84.6	1.8	85.2	1.8	85.0
Ag^2	86.7	1.2	95.2	0.7	84.0
Ag^3	97.5	1.3	101	0.8	93.8
Bg^3	100	1.0	—	—	95.2
Bg^4	111	2.3	116	2.0	101.2
Ag^4	116	2.9	121	2.5	98.2
Bg^5	119	2.2	—	—	115.4
Ag^5	141	0.1	144	0.4	144.0
Ag^6	145	3.5	151	3.0	151.3
Bg^6	154	0.2	—	—	119.1
Bg^7	161	1.1	161[b]	2.8	158
Ag^7	165	0.8	161[b]	2.8	158
Bg^8	166	2.0	171	2.4	170.7
Ag^8	186	2.4	196	2.1	195.9
Bg^9	188	2.4	—	—	205.4
Ag^9	194	0.6	—	—	—
Bg^{10}	204	−1.3	206	−0.3	237.7
Bg^{11}	216	6.3	—	—	261.3
Ag^{10}	227	3.7	237	3.3	237.7
Bg^{12}	242	6.3	—	—	261.3
Ag^{11}	249	4.3	260	3.8	—
Bg^{13}	249	5.0	—	—	—
Ag^{12}	275	4.3	297	2.9	296.9
Bg^{14}	283	3.9	—	—	296.9
Ag^{13}	316	2.6	330	2.3	—
Bg^{15}	332	4.6	—	—	329.1
Ag^{14}	333	4.7	347	3.4	338.7
Bg^{16}	347	4.7	—	—	359.7
Ag^{15}	349	5.1	360	4.8	347.3
Bg^{17}	361	5.9	—	—	363.4
Ag^{16}	367	6.6	—	—	383.4
Bg^{18}	375	4.6	—	—	392.1
Ag^{17}	380	4.5	385	3.6	400.5
Bg^{19}	385	4.5	—	—	418.8
Ag^{18}	387	3.7	400	2.4	418.8
Bg^{20}	473	−2.8	441[c]	4.6	478.7
Ag^{19}	476	−2.7	474[c]	2.2	478.7
Bg^{21}	691	7.9	719[b]	5.5	720.9
Ag^{20}	693	7.7	719[b]	5.5	739.7
Ag^{21}	714	9.5	741[b]	5.7	773.6
Bg^{22}	716	8.8	741[b]	5.7	785.1
Bg^{23}	763	4.1	774	3.9	816.8
Ag^{22}	772	4.2	785	3.5	816.8
Ag^{23}	800	2.0	817	2.2	842.5
Bg^{24}	822	2.0	843	1.8	842.5
Bg^{25}	868	3.3	—	—	913.8
Bg^{26}	890	1.4	—	—	913.8
Ag^{24}	893	1.5	902	2.1	901.4
Ag^{25}	910	0.5	913	1.7	—

[a] Ref. [16].

[b] These modes can be either of Ag or of Bg modes.

[c] These modes can be second order modes.

observed for the Raman-active modes in the three regions (see Table 1). Below 200 cm^{-1}, Raman-active modes have the smallest pressure coefficients (below 3.5 cm^{-1}/GPa). Between 200 and 500 cm^{-1} Raman modes have pressure coefficients between 2.6 and 6.6 cm^{-1}/GPa. Finally, the pressure coefficients of the stretching modes range from 0.5 to 9.5 cm^{-1}/GPa. This behavior is similar to that found in scheelite-type molybdates and tungstates [39, 40]. Furthermore, when analyzing the pressure dependence of the Raman-active modes of $Eu_2(MoO_4)_3$, it can be observed that many Raman-active modes in trimolybdates are grouped into Ag and Bg pairs with similar frequencies (and in many cases) similar behavior with increasing pressure. Most of these pairs are related to Eg modes of the parent scheelite structure [39, 40]. In particular, the two bending modes with largest frequency (around 470 cm^{-1} according to our calculations) and the four stretching modes with lowest frequency (around 700 cm^{-1} according to our calculations) derive from the Eg modes of the scheelite structure. Furthermore, these pair modes in trimolybdates are weakly observed in Raman scattering as the Eg modes of the scheelite structure in molybdates.

3.4. Eu^{3+} surrounding

To improve our experimental knowledge of the pressure dependence for the coordination polyhedra, we have taken advantage of the relatively simple diagram of Eu^{3+} ion levels and the high dependence of its photoluminescence on its surrounding. In the already mentioned study by Atuchin *et al* [16], they also characterized the photoluminescence spectrum of α-$Eu_2(MoO_4)_3$ at ambient conditions. Based on that study, we have analyzed the pressure evolution of the photoluminescence spectrum.

In our experiments at AP, the emission spectrum has been obtained exciting at 395 nm (25316 cm^{-1}) in resonance with the $^7F_0 \rightarrow ^5L_6$ transition. Different peaks corresponding to the $^5D_0 \rightarrow ^7F_J$ (J=0–4) transitions can be identified in the emission spectra. The $^5D_0 \rightarrow ^7F_0$ transition gives a single narrow peak at 580.3 nm (see Fig. 7), indicating that all the Eu^{3+} ions occupy exactly the same local surrounding in the α-$Eu_2(MoO_4)_3$ structure at AP, despite the lack of symmetry of their surroundings. Moreover, no other peaks belonging to sites of a different structural phase are found. The $^5D_0 \rightarrow ^7F_1$ (585–605 nm) transition shows three overlapped peaks (see Fig. 8), indicating the low symmetry of the Eu^{3+} surroundings in the trimolybdate crystal [41].

To obtain more information about the effect of the volume compression on the local surroundings of the Eu^{3+} ions, the present study has been limited to the analysis of the photoluminescence spectra associated with the $^5D_0 \rightarrow ^7F_J$ transitions (J=0, 1) which is expected to show higher sensitivity to changes in the Eu^{3+}–O^{2-} bond length and angles. As pointed out by Machon *et al* [17], the literature data show that the down-shift of the $^5D_0$ lowest emitting level with pressure is much faster than for the ^7F_J multiplets, whose Stark levels change non-uniformly in energy, giving rise to an overall red-shift of the photoluminescence with pressure. Note that, within the range of pressures from ambient conditions up to 14.6 GPa, there are no discontinuities in spectral

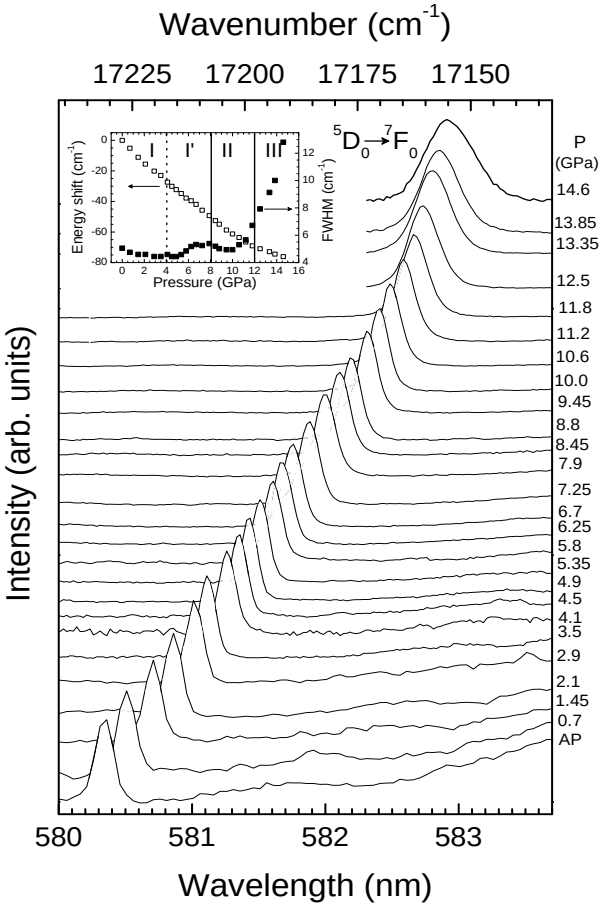

Figure 7. Emission spectra to the $^5D_0 \rightarrow ^7F_0$ transition of α-$Eu_2(MoO_4)_3$ at different pressures. The inset shows the peak position and the FWHM for this transition. Vertical lines are used to distinguish three regions with different tendency.

parameters such as the number of lines, evolution of the frequencies, or intensity with pressure. Thus, in our experiments there are not strong variations of the Eu^{3+}–O^{2-} bond distances or angles and, hence, we do not observe any pressure-induced transition to a different crystalline phase. Discontinuities were not observed in the emission of Eu^{3+} doped α-$Gd_2(MoO_4)_3$ up to 25 GPa [42]. However, for the β'-$Eu_2(MoO_4)_3$, some discontinuities have been found by Machon *et al* [17] when describing the structural phase transitions and PIA.

The effects of pressure on the $^5D_0 \rightarrow ^7F_0$ transition have been addressed by measuring in detail the emission between these singlet (non-degenerated) levels from AP up to 14.6 GPa (see Fig. 7). Antic *et al* [43] clearly show that the $^5D_0$ state of Eu^{3+} has little or no correlation with parameters such as bond length and coordination number. However, the use of the variations of the energy of the $^5D_0 \rightarrow ^7F_0$ transition to assess the overall covalency of the Eu^{3+}–O^{2-} bonds is reasonable in the case of the α-$Eu_2(MoO_4)_3$ crystals, since both the nature of the ligands and the local structure are expected to vary gradually with pressure. On the other side, the comparison of the

variations of the full width at half maximum (FWHM) of this peak at high pressure with respect to the value at AP can be used as a fingerprint of the initial stages of an increase of the number of Eu^{3+} sites in the crystal, and hence, the beginning of the amorphization.

Taking into account the values obtained for the red-shift and the FWHM of the $^5D_0 \rightarrow ^7F_0$ peak plotted in the inset of Fig. 7, three different pressure stages can be clearly observed:

(i) The first stage, from ambient pressure to 8 GPa, can be divided in two sub-stages with minor changes: I) from ambient to around 4 GPa the emission shows a single and narrow peak that shifts to the red (i.e. to lower energies) with a quasi-linear rate of approximately -6.5 cm^{-1}/GPa (0.22 nm/GPa), while the FWHM slightly decreases ($\sim$ 0.6 cm^{-1}); and I') from 4 to 8 GPa, with an inflection point for both the red-shift, which decreases to -5.5 cm^{-1}/GPa (0.18 nm/GPa), and the FWHM, that slightly increases around 1 cm^{-1} to decrease again to its initial value at ambient pressure. The two sub-stages (I and I') of pressure give more or less the same results, with really slight variations of the red-shift rate and the peak width, indicating that only minor Eu^{3+} site symmetry structural changes take place between AP and 8 GPa, accompanied by an overall increase of covalency for the Eu^{3+}–O^{2-} bonds.

(ii) In the second stage from 8 up to 12 GPa, the red-shifting and the broadening of the FWHM are clearly non-linear. The FWHM reaches similar values at the measured extreme pressures of this stage (7.9 and 11.8 GPa). Both effects can only be ascribed to an amorphization of the α-$Eu_2(MoO_4)_3$ crystals. With increasing pressure, the broadening increases and simultaneously a broad shoulder appears at the high-energy side of the $^5D_0 \rightarrow ^7F_0$ peak. These effects are associated to the generation of different surroundings for the Eu^{3+} ions in stronger crystal-field environments as a result of the compression and further distortions of the original Eu-ligand bond distances and angles of the local surrounding at AP, which we call the "original" Eu^{3+} site. While a similar red-shifting rate is expected for this "original" Eu^{3+} site, pressure generates new distorted sites for the Eu^{3+} ions, especially with stronger crystal-field strengths, and whose $^5D_0 \rightarrow ^7F_0$ energies are blue-shifted by the J-mixing interaction [44, 45]. The proximity of the $^7F_1$ and $^7F_2$ multiplets compared to the energy separation between the $^5D_0$ and the $^5D_2$ multiplets have suggested to Nishimura *et al* [46] that the inhomogeneous broadening of the $^5D_0 \rightarrow ^7F_0$ peak is mainly due to the downward energy shift of the $^7F_0$ level induced by the J-mixing. These results indicate an increase in the fluctuation of the local structures and crystal-field strengths due to differences in the Eu-ligand bond distances and angles that results in a large variety of surroundings and a broadening of the $^5D_0 \rightarrow ^7F_0$ peak, which becomes a band, but without a significant shift. Thus, at the second stage of pressures between 8 and 12 GPa, these new stronger crystal-field sites would start to be created. At around 10.5 GPa there is an inflection point in the pressure dependence of several bond lengths, angles and lattice parameters. This

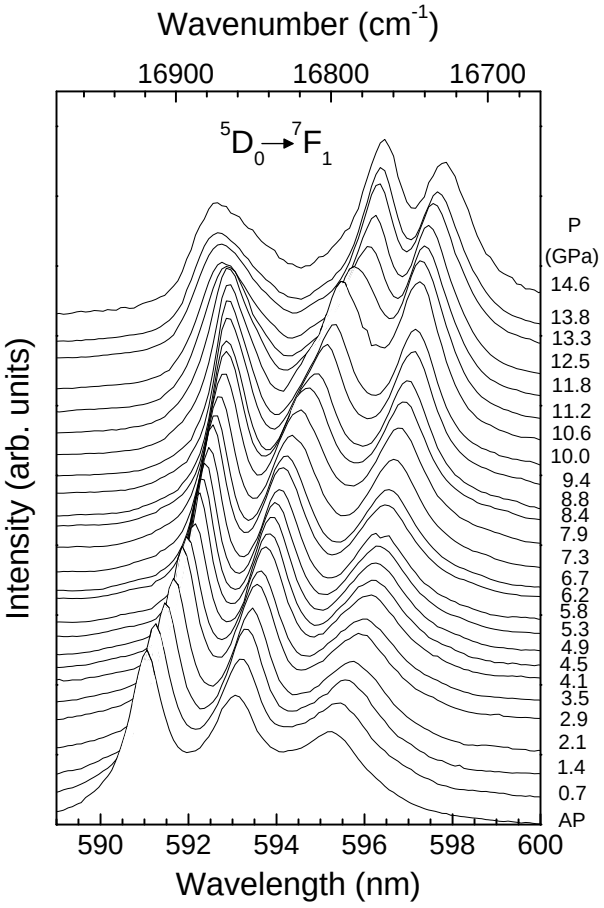

Figure 8. Emission spectra to the transition $^5D_0 \rightarrow ^7F_1$ of α-$Eu_2(MoO_4)_3$ at different pressures.

produces abrupt structural changes which may lead to the amorphization.

(iii) Finally, starting from 12 GPa, the evolution of the structural parameters becomes more monotonous under pressure and the PIA begins.

The three pressure stages found analyzing the $^5D_0 \rightarrow ^7F_0$ emission can be correlated with the results obtained for the $^5D_0 \rightarrow ^7F_1$ transition. The analysis of the pressure dependence of the $^5D_0 \rightarrow ^7F_2$ transition is more complex and is not included in the present work. Fig. 8 shows the $^5D_0 \rightarrow ^7F_1$ transition as a function of pressure. Since the $^5D_0$ levels are a singlet, the positions of the $^7F_1$ Stark levels with respect to the $^7F_0$ ground level are collected and plotted as a function of pressure in Fig. 9. Three different pressure stages can be observed when the positions of the three peaks of the $^5D_0 \rightarrow ^7F_1$ transition are analyzed. The first stage is subdivided in two stages with minor changes: I) up to 4 GPa, where these three peaks also shift to the red as the $^5D_0 \rightarrow ^7F_0$ but, at the same time, the two highest energy peaks (lowest energy Stark levels) start to reduce the gap between them, resulting in a slow decrease of the $^7F_1$ multiplet's splitting; and I') up to 8 GPa, where only the red-shifting is appreciable, with an almost constant splitting. The second stage (II) begins at 8 GPa, when the two highest energy peaks

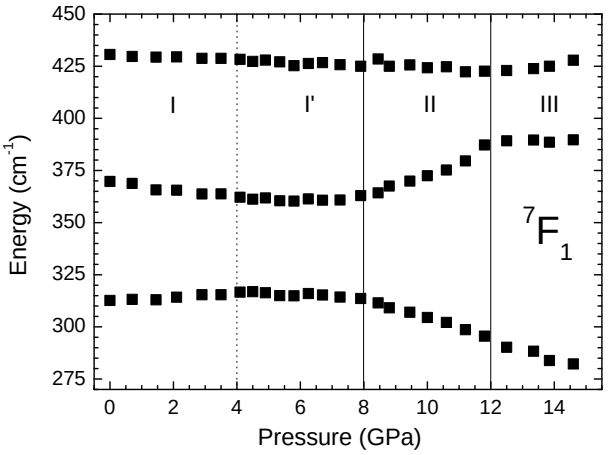

Figure 9. Shifts of the $^7F_1$ Stark levels with respect to $^7F_0$ ground level at all measured pressures. Vertical lines are used to distinguish three regions with different tendency.

start to rapidly separate in energy with opposite directions, the highest energy peak is moved to the blue, and the central one to the red, both increasing the splitting and their FWHM till 12 GPa, indicating abrupt changes in the Eu^{3+} surrounding. Finally, the third stage (III) develops above this pressure of 12 GPa, where less changes are observed and the amorphization clearly proceeds. All these changes in the energies of the $^7F_1$ Stark levels can be directly correlated with changes in the crystal-field strength felt by the Eu^{3+} ions under pressure and these three stages are completely correlated with the compression of the crystal structure and the Raman phonons.

4. Conclusions

We have performed an exhaustive study on the behavior of the α-phase of europium trimolybdate under high pressure. A good agreement between results from several experimental techniques and theoretical calculation was found in the whole range of pressures. As a result, we have improved previous results where the amorphization process in the α- and β'-phases was not well differentiated.

According to the present study, from AP to 8 GPa, the compression is monotonous, uniform and isotropic. In contrast, within the pressure interval between 8 and 12 GPa, we observe anomalies in the crystal structure, and also in the evolution of the Raman and photoluminescence peaks although without any clear indication of crystalline-crystalline phase transitions. To our knowledge, these anomalies have not been previously explained. This behavior has been monitored theoretically and it can be owed to an anisotropic compression of the MoO_4 tetrahedra and modifications in the Eu surrounding, resulting in a more compact packing of the structure. This is compatible with the pressure evolution of the experimental cell parameters, phonons, and photoluminescence peaks.

We set the beginning of the amorphization at approximately 12 GPa, when the

rate of compression of the crystal structure becomes smaller: at this pressure, there is a change in the slope of the pressure dependence for the structural parameters, phonon, and emission-peak frequencies. Moreover, an increase of the number of Eu^{3+} sites, which translates into stronger crystal fields, can be predicted by the broadening of the $^5D_0 \rightarrow ^7F_0$ emission line and the decrease of the energy red-shifting, among other effects. The onset of the PIA can be confirmed by the broadening of the Raman peaks and, finally, by their extinction at 21 GPa.

This compression process contrasts with the results of other compounds with the same structure at AP. On the one hand, α-$La_2(WO_4)_3$ undergoes two phase transitions before its amorphization, which is irreversible. On the other hand, the unit cell of α-$Tb_2(MoO_4)_3$ compresses by decreasing the monoclinic β-angle and its amorphization is confirmed by X-ray diffraction at pressures above 21 GPa. We are conducting further structural studies on several related compounds featuring the α-phase, with the objective of understanding the different mechanisms in which the PIA develops and its degree of reversibility. We believe these studies will also provide information on new distinct structural effects thanks to the comparison of the behavior of the α-phase with that of the better known β'-phase.

Acknowledgments

We thank Diamond Light Source for access to *beamline I15* (EE1746) that contributed to the results presented here. Part of the diffraction measurements were performed at the "Servicio Integrado de Difracción de Rayos X (SIDIX)" of University of La Laguna. This work has been supported by Ministerio de Economía y Competitividad of Spain (MINECO) for the research projects through the National Program of Materials (MAT2010-21270-C04-01/02/03/04, MAT2013-46649-C4-1/2/3/4-P and MAT2013-43319-P), the Consolider-Ingenio 2010 MALTA (CSD2007-00045), the project of Generalitat Valenciana (GVA-ACOMP/2014/243) and by the European Union FEDER funds. C. Guzmán-Afonso wishes to thank ACIISI and FSE for a fellowship. J. A. Sans thanks the FPI and "Juan de la Cierva" programs for fellowships.

References

[1] Globus M, Grinyov B and Kim J K 2005 *Inorganic Scintillators for Modern and Traditional Applications* (Kharkov: Institute for Single Crystals)
[2] Kaczmarek A M and Van Deun R 2013 *Chem. Soc. Rev.* **42** 8835
[3] Lin C C and Liu R S 2011 *J. Phys. Chem. Lett.* **2** 1268
[4] Templeton D H and Zalkin A 1963 *Acta Crystallogr.* **16** 762
[5] Martinez-Garcia J, Arakcheeva A, Pattison P, Morozov V and Chapuis G 2009 *Philosophical Magazine Letters* **89** 257
[6] Keve E T, Abrahams S C and Bernstein J L 1971 *J. Chem. Phys.* **54** 3185
[7] Brixner L H, Barkley J R and Jeitschko W 1979 *Handbook on the Physics and Chemistry of Rare Earth* (Amsterdam: North-Holland)

[8] Jayaraman A, Sharma S K, Wang Z, Wang S Y, Ming L C and Manghnani M H 1993 *J. Phys. Chem. Solids* **54** 827

[9] Dmitriev V, Sinitsyn V, Dilanian R, Machon D, Kuznetsov A, Ponyatovsky E, Lucazeau G and Weber H P 2003 *J. Phys. Chem. Solids* **64** 307

[10] Lucazeau G, Le Bacq O, Pasturel A, Bouvier P and Pagnier T 2011 *J. Raman Spectrosc.* **42** 452

[11] Guzmán-Afonso C, López-Solano J, González-Silgo C, León-Luis S F, Matesanz E and Mujica A 2014 *High Pressure Res.* **34** 184

[12] Jayaraman A, Sharma S K, Wang Z and Wang S Y 1997 *Solid State Commun.* **101** 237

[13] Le Bacq O, Machon D, Testemale D and Pasturel A 2011 *Phys. Rev. B* **83** 214101

[14] Maczka M, Filho A G S, Paraguassu W, Freire P T C, Filho J M and Hanuza J 2012 *Prog. Mater. Sci.* **57** 1335

[15] Sabalisck N P, López-Solano J, Guzmán-Afonso C, Santamaría-Pérez D, González-Silgo C, Mujica A, Muñoz A, Rodríguez-Hernández P, Radescu S, Vendrell X, Mestres L, Sans J A and Manjón F J 2014 *Phys. Rev. B* **89** 174112

[16] Atuchin V V, Aleksandrovsky A S, Chimitova O D, Gavrilova T A, Krylov A S, Molokeev M S, Oreshonkov A S, Bazarov B G and Bazarova J G 2014 *J. Phys. Chem. C* **118** 15404

[17] Machon D, Dmitriev V P, Sinitsyn V V and Lucazeau G 2004 *Phys. Rev. B* **70** 094117

[18] Guzmán-Afonso C, Torres M E, González-Silgo C, Sabalisck N, González-Platas J, Matesanz E and Mujica A 2011 *Solid State Commun.* **151** 1654

[19] Mao H K, Bell P M, Shaner J W and Steinberg D J 1978 *J. Appl. Phys.* **49** 3276

[20] Mao H K, Xu J and Bell P M 1986 *J. Geophys. Res.: Solid Earth* **91** 4673

[21] Hammersley A P, Svensson S O, Hanfland M, Fitch A N and Hausermann D 1996 *High Pressure Res.* **14** 235

[22] Le Bail A 2005 *Powder Diffr.* **20** 316

[23] Rodríguez-Carvajal J 1993 *Physica B* **192** 55

[24] Hohenberg P and Kohn W 1964 *Phys. Rev.* **136** B864

[25] Kresse G and Furthmüller J 1996 *Phys. Rev. B* **54** 11169

[26] Kresse G and Joubert D 1999 *Phys. Rev. B* **59** 1758

[27] Blöchl P E 1994 *Phys. Rev. B* **50** 17953

[28] Perdew J P, Ruzsinszky A, Csonka G I, Vydrov O A, Scuseria G E, Constantin L A, Zhou X and Burke K 2008 *Phys. Rev. Lett.* **100** 136406

[29] Dudarev S L, Botton G A, Savrasov S Y, Humphreys C J and Sutton A P 1998 *Phys. Rev. B* **57** 1505

[30] Chetty N, Muoz A and Martin R M 1989 *Phys. Rev. B* **40** 11934

[31] Mujica A, Rubio A, Muñoz A and Needs R J 2003 *Rev. Mod. Phys.* **75** 863

[32] Parlinski K 2008 software phonon URL `http://wolf.ifj.edu.pl/phonon/`

[33] Errandonea D, Muñoz A and Gonzalez-Platas J 2014 *J. Appl. Phys.* **115** 216101

[34] Gomis O, Sans J A, Lacomba-Perales R, Errandonea D, Meng Y, Chervin J C and Polian A 2012 *Phys. Rev. B* **86** 054121

[35] Vilaplana R, Lacomba-Perales R, Gomis O, Errandonea D and Meng Y 2014 *Solid State Sci.* **36** 16

[36] Klotz S, Chervin J C, Munsch P and Marchand G L 2009 *J. Phys. D: Appl. Phys.* **42** 075413

[37] Brown I D and Altermatt D 1985 *Acta Crystallogr., Sect. B* **41** 244

[38] Boulahya K, Parras M and González-Calbet J M 2005 *Eur. J. Inorg. Chem.* **2005** 967

[39] Manjón F J, Errandonea D, Garro N, Pellicer-Porres J, Rodríguez-Hernández P, Radescu S, López-Solano J, Mujica A and Muñoz A 2006 *Phys. Rev. B* **74** 144111

[40] Vilaplana R, Gomis O, Manjón F J, Rodríguez-Hernández P, Muñoz A, Errandonea D, Achary S N and Tyagi A K 2012 *J. Appl. Phys.* **112** 103510

[41] Görller-Walrand C and Binnemans K 1996 *Rationalization of crystal-field parametrization* vol 23 (Amsterdam: Elsevier Science B.V.) in Handbook on the Physics and Chemistry of Rare Earths

[42] Mahlik S, Lazarowska A, Grobelna B and Grinberg M 2012 *J. Phys.: Condens. Matter* **24** 485501

[43] Antic-Fidancev E, Lemaître-Blaise M and Caro P 1987 *New J. Chem.* **11** 467
[44] Nishimura G and Kushida T 1988 *Phys. Rev. B* **37** 9075
[45] Lavín V, Rodríguez-Mendoza U R, Martín I R and Rodríguez V D 2003 *J. Non-Cryst. Solids* **319** 200
[46] Nishimura G and Kushida T 1991 *J. Phys. Soc. Jpn.* **60** 683